Supporting Information

Zhang et al. 10.1073/pnas.1717219115

As illustrated in Fig. 1 *E* and *F*, there are two adsorption sites at the surface of M_2C, which correspond to site i: HCP hollow site (stack as ABABAB...) and site ii: FCC hollow site (stack as ABCABC...), respectively. The two absorption sites will generate three configurations denoted as I, II, and III (Fig. S1 *A*–*C*), which correspond to the functional groups being absorbed at pure site i, at pure site ii, and at both sites, respectively. It can be seen from Table S1 that the configuration II of Ti_2CT_2(T = F,O) has the lowest adsorption energy, in agreement with previous studies (1).

1. Tang Q, Zhou Z, Shen P (2012) Are MXenes promising anode materials for Li ion batteries? Computational studies on electronic properties and Li storage capability of Ti_3C_2 and $Ti_3C_2X_2$ (X = F, OH) monolayer. *J Am Chem Soc* 134:16909–16916.

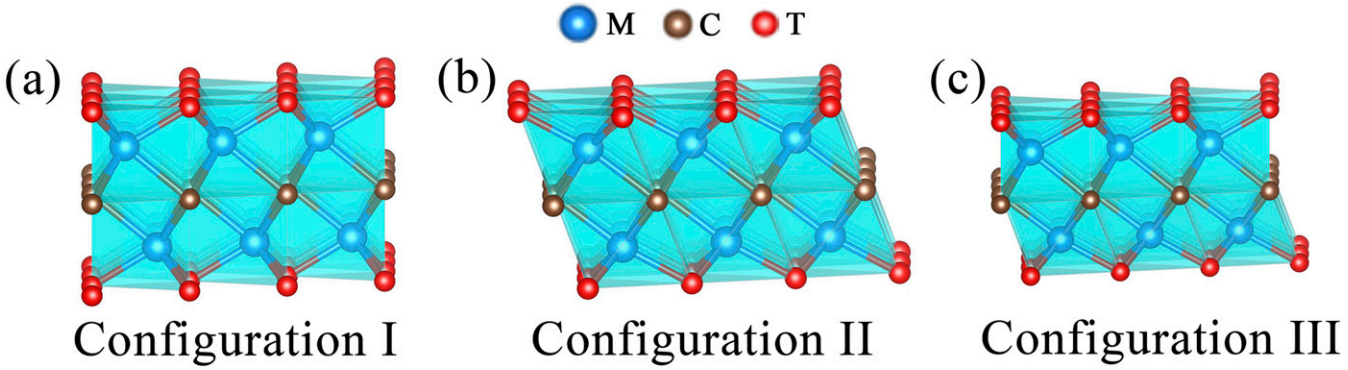

Fig. S1. (*A*–*C*) The atomic structures in configurations I, II, and III of M_2CT_2 (T = O, F), respectively.

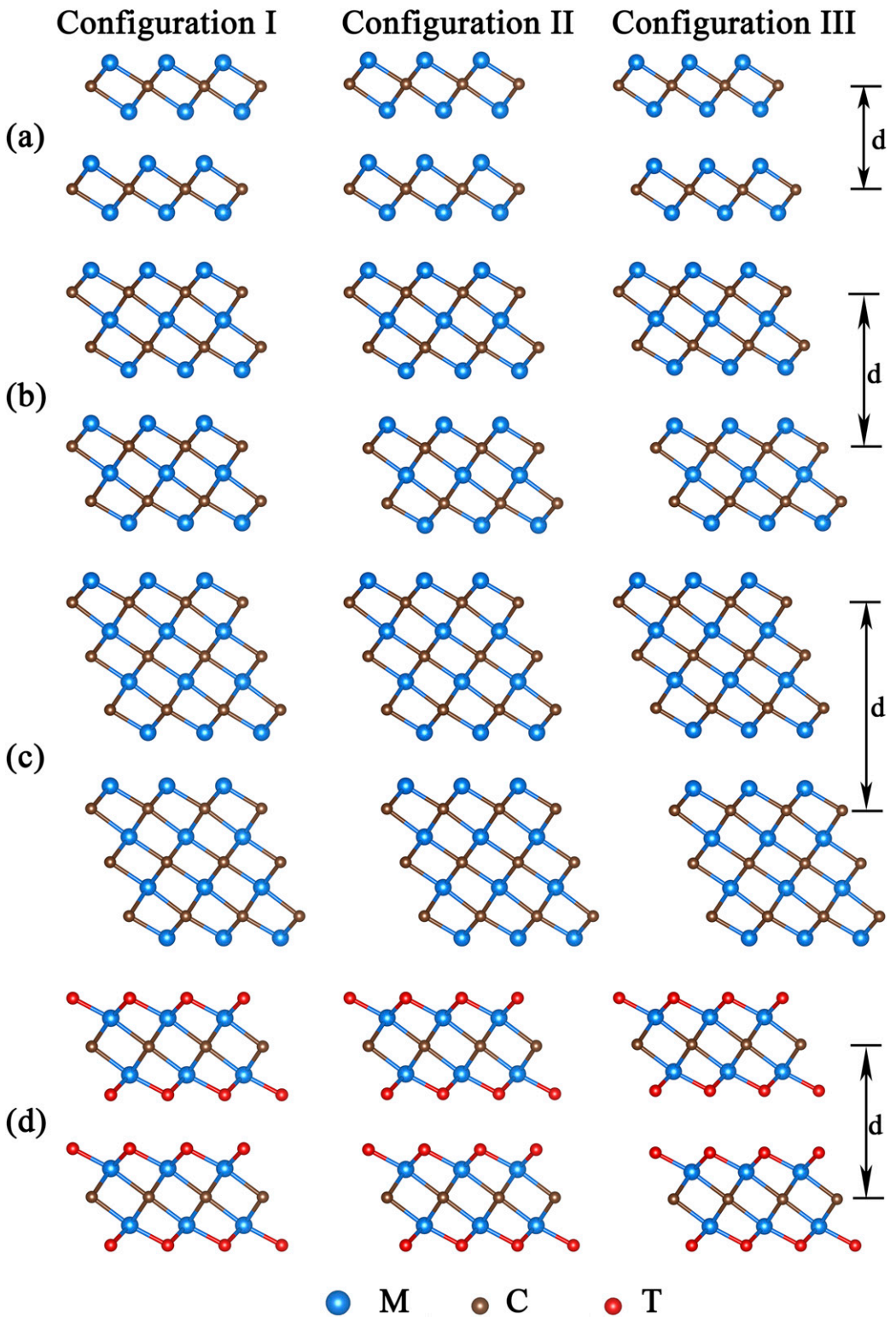

Fig. S2. Side view of (*A*) M_2C, (*B*) M_3C_2, (*C*) M_4C_3, and (*D*) M_2CT_2 in three distinct stacking types that correspond to configurations I, II, and III, respectively. In configuration I, the atoms of the top layer point to the hollow site 1 of their counterparts in the neighboring layer. In configuration II, the atoms of the top layer point to the hollow site 2 of their counterparts in the neighboring layer. In configuration III, the adjacent layers are arranged in a face-to-face manner. Hollow site 1 is the site on top of the second layer, while hollow site 2 is the site on top of the third layer.

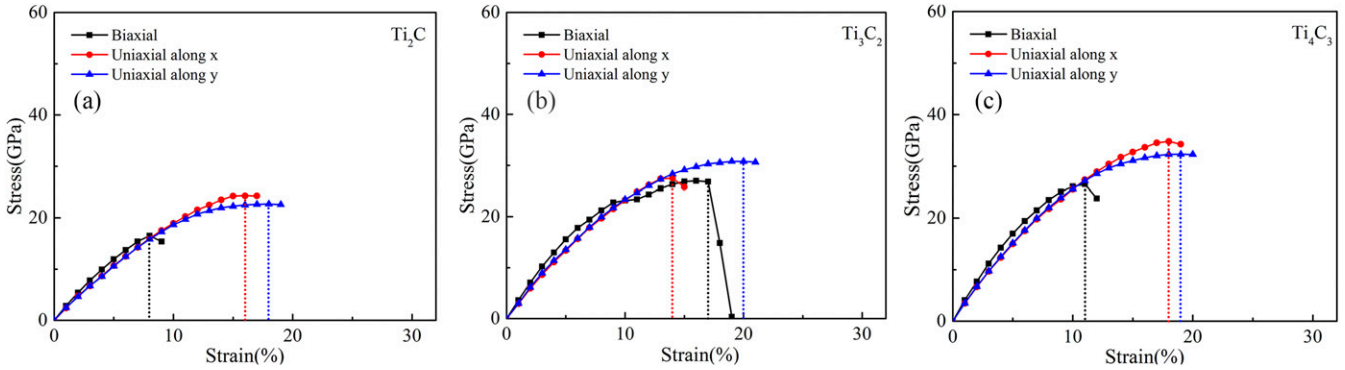

Fig. S3. The strain-stress relations for (*A*) Ti_2C, (*B*) Ti_3C_2, and (*C*) Ti_4C_3 under both biaxial and uniaxial load conditions.

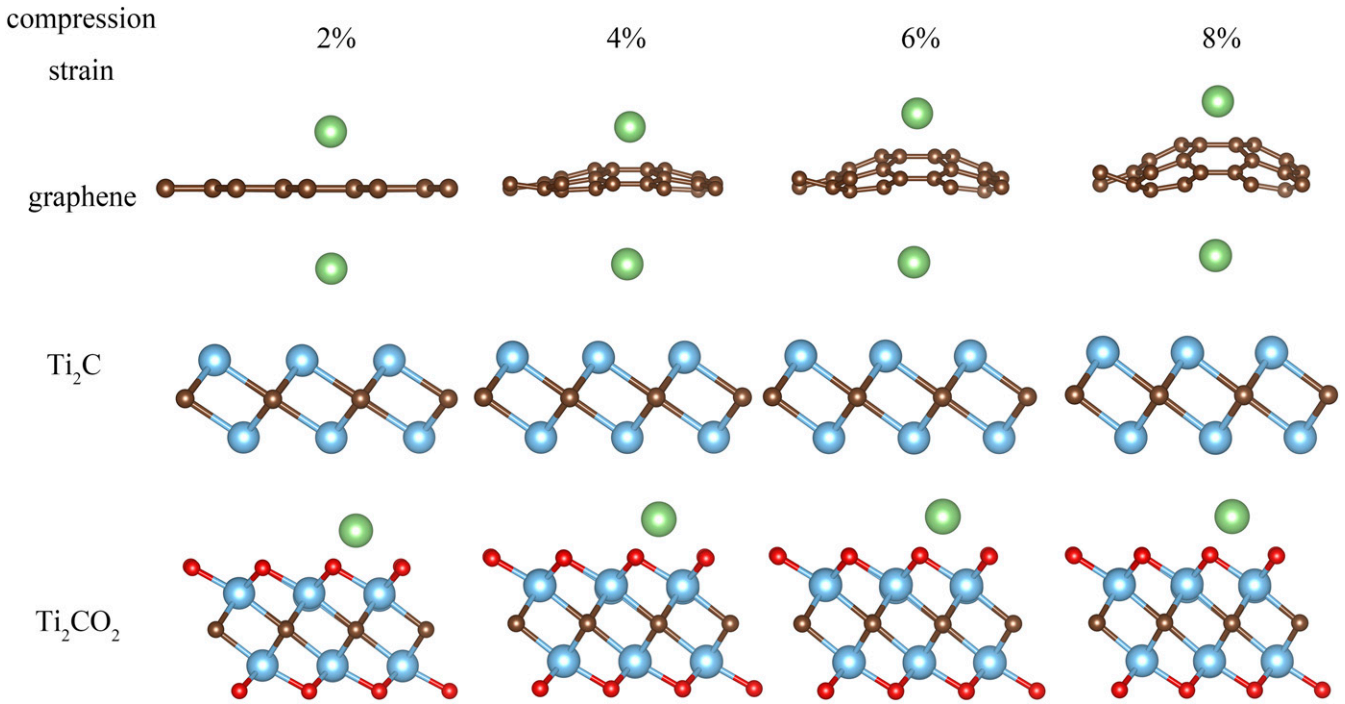

Fig. S4. The atomic structures of Li adsorbing on graphene, Ti_2C, and Ti_2CO_2 under 2%, 4%, 6%, and 8% compression strain.

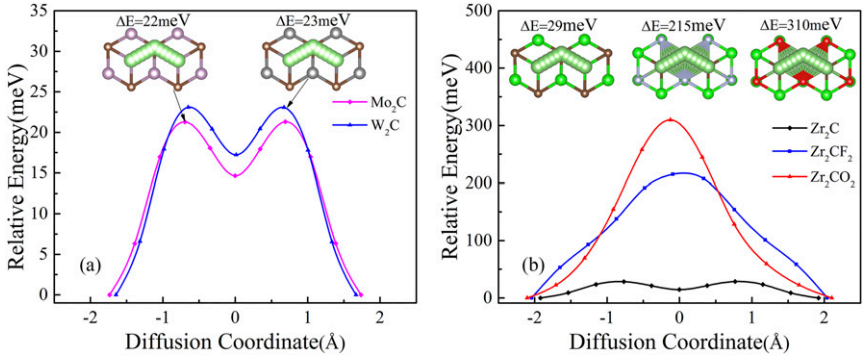

Fig. S5. Potential-energy profiles of Li^+ diffusion on the charged surface of (*A*) Mo_2C and W_2C and (*B*) Zr_2C, Zr_2CF_2, and Zr_2CO_2.

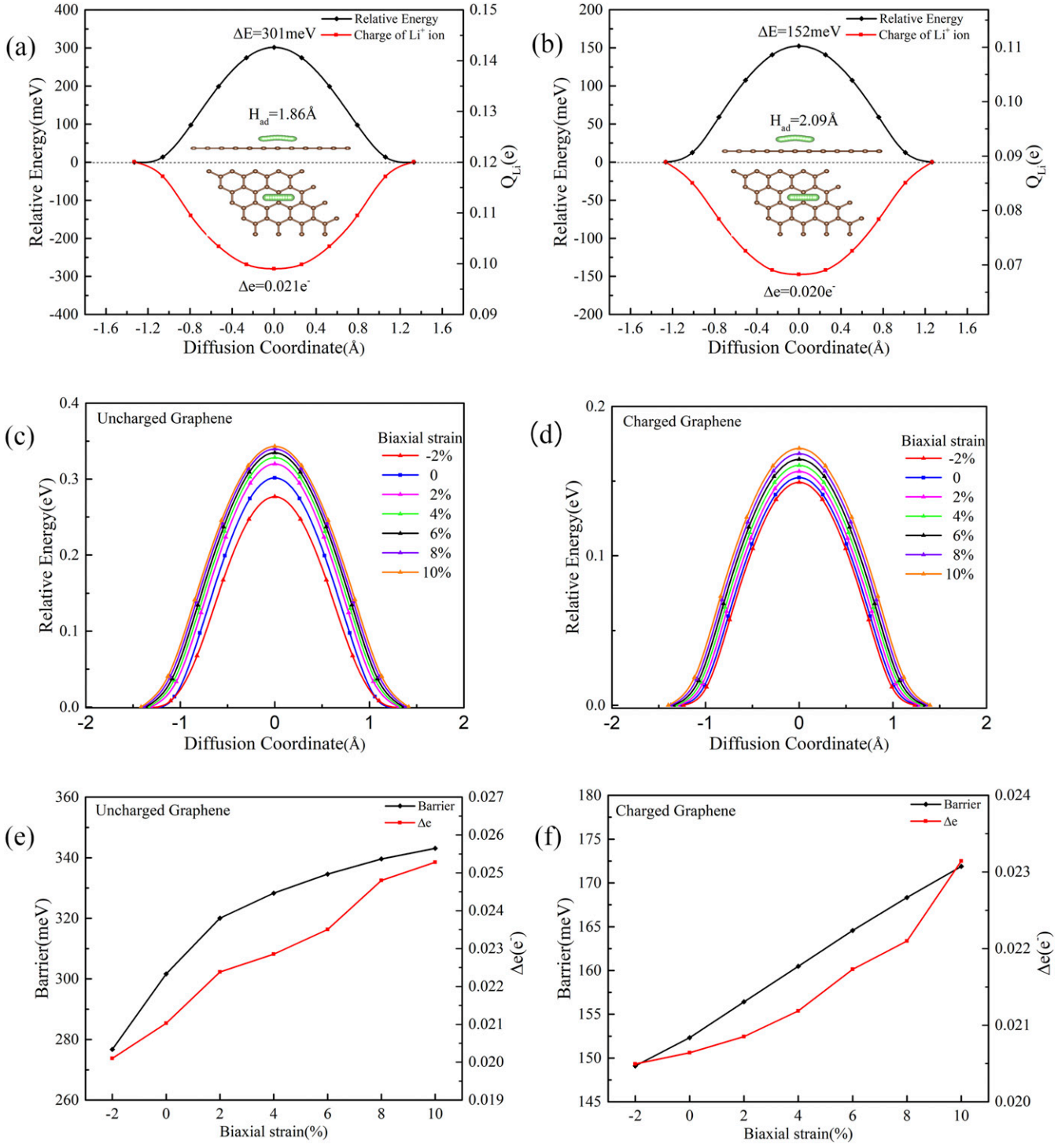

Fig. S6. Relative energy, charge, and adsorption height of Li^+ diffusion on (*A*) uncharged and (*B*) charged graphene. Potential-energy curves of Li^+ diffusion on (*C*) uncharged and (*D*) charged graphene under biaxial strains. Charge differences Δe and barriers of Li^+ on (*E*) uncharged and (*F*) charged graphene as a function of biaxial strain.

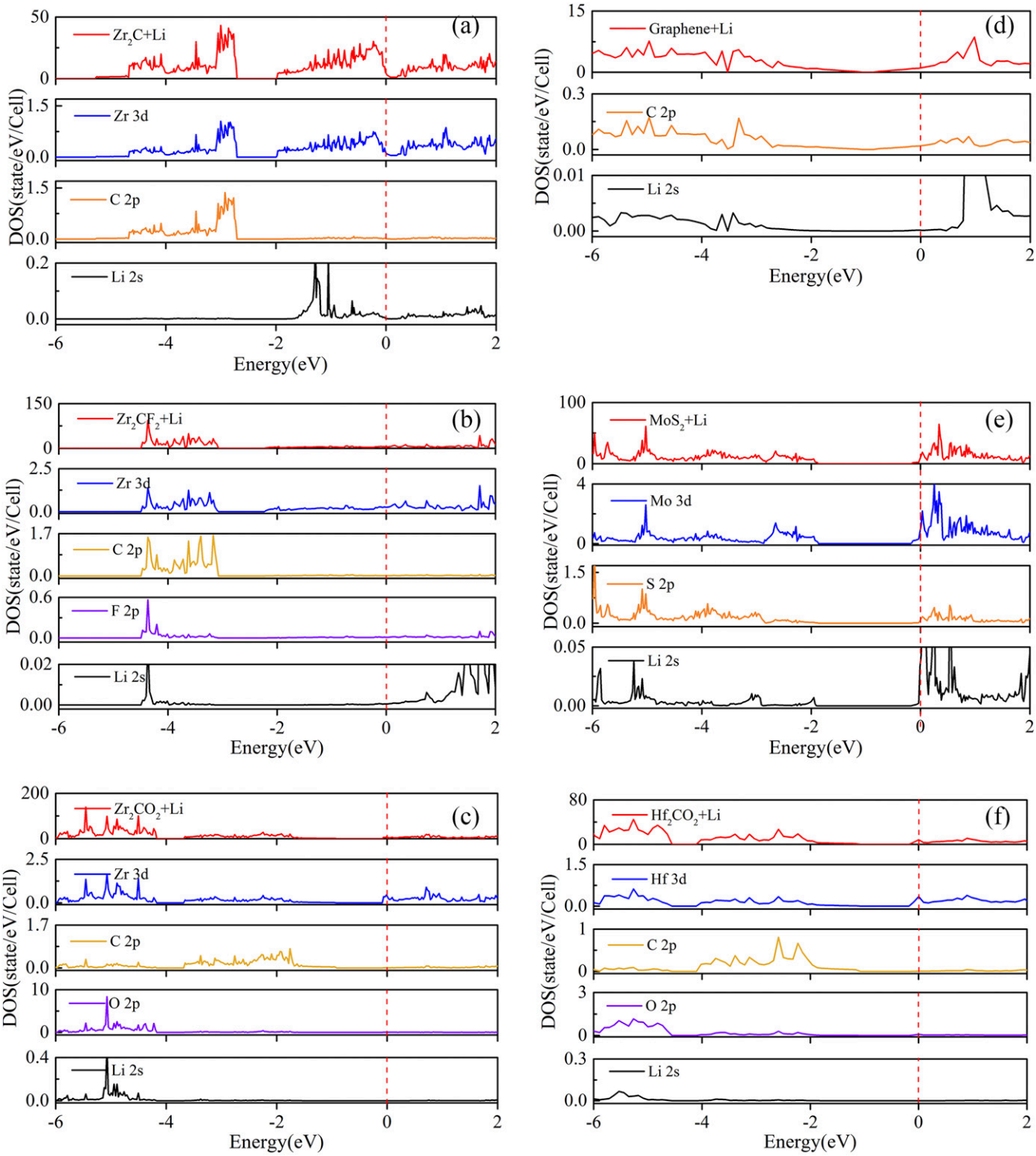

Fig. S7. Total DOS and PDOS of Li on (*A*) Zr_2C, (*B*) Zr_2CF_2, (*C*) Zr_2CO_2, (*D*) graphene, (*E*) MoS_2, and (*F*) Hf_2CO_2. The Fermi levels are set to zero and indicated by the dashed lines.

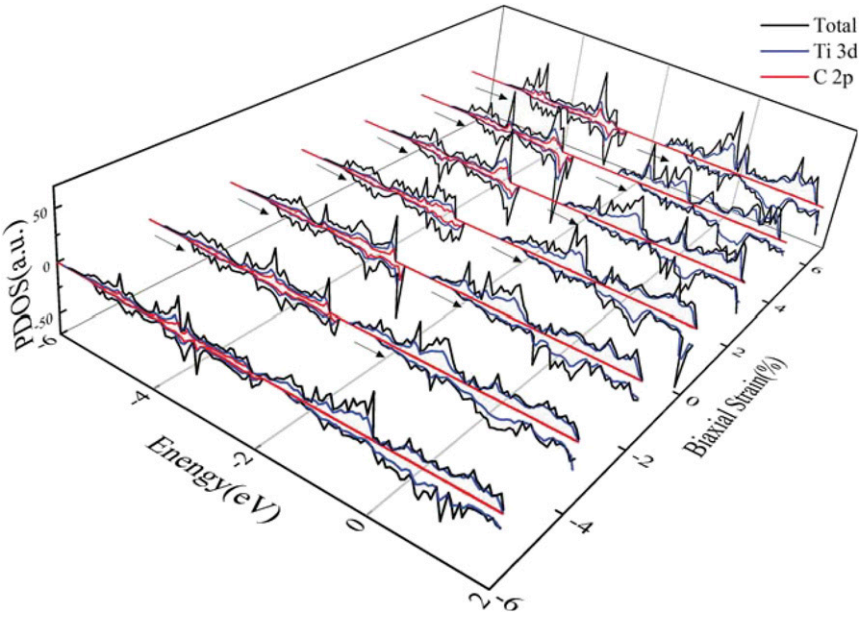

Fig. S8. PDOS of Ti_2C under different biaxial strains.

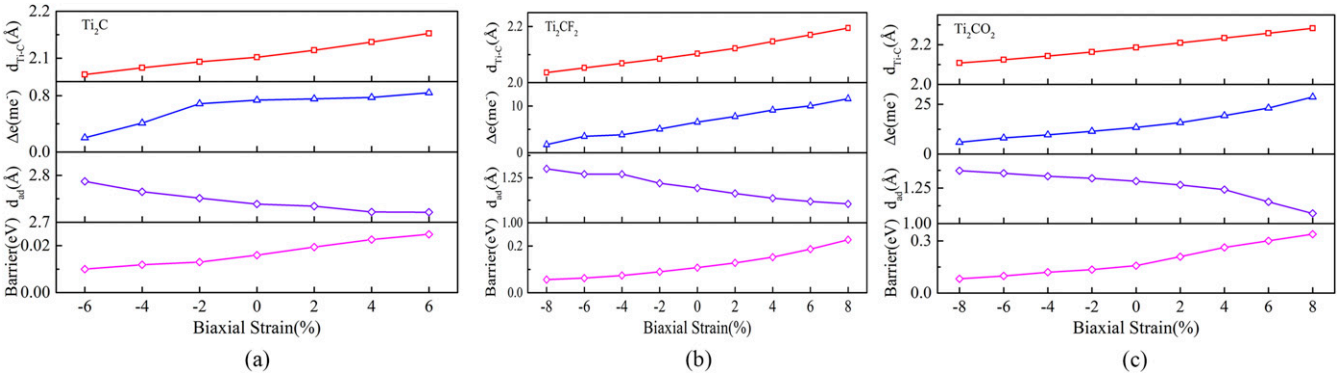

Fig. S9. Bond length $d_{Ti\text{-}C}$, charge difference Δe, adsorption height d_{ad}, and barrier of (*A*) Ti_2C, (*B*) Ti_2CF_2, and (*C*) Ti_2CO_2 as a function of biaxial strain.

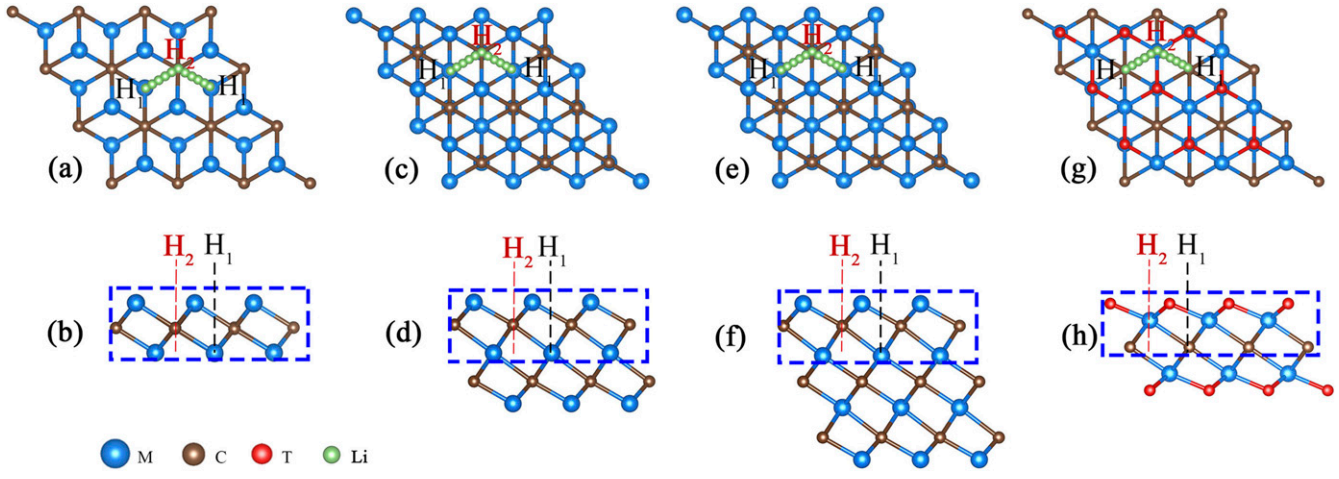

Fig. S10. Top views of (*A*) M_2C, (*C*) M_3C_2, (*E*) M_4C_3, and (*G*) M_2CT_2 and side views of (*B*) M_2C, (*D*) M_3C_2, (*F*) M_4C_3, and (*H*) M_2CT_2. H_1 and H_2 represent FCC hollow and HCP hollow, respectively. The diffusion paths of Li^+ are schematically shown in top views.

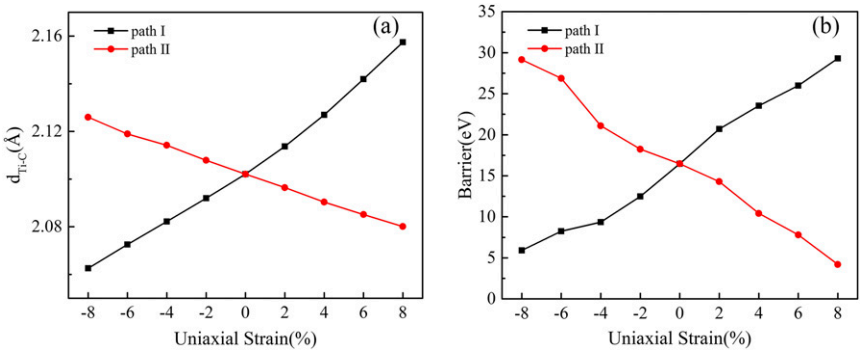

Fig. S11. Bond length d_{Ti-C} (*A*) and barrier (*B*) of Ti_2C as a function of uniaxial strain.

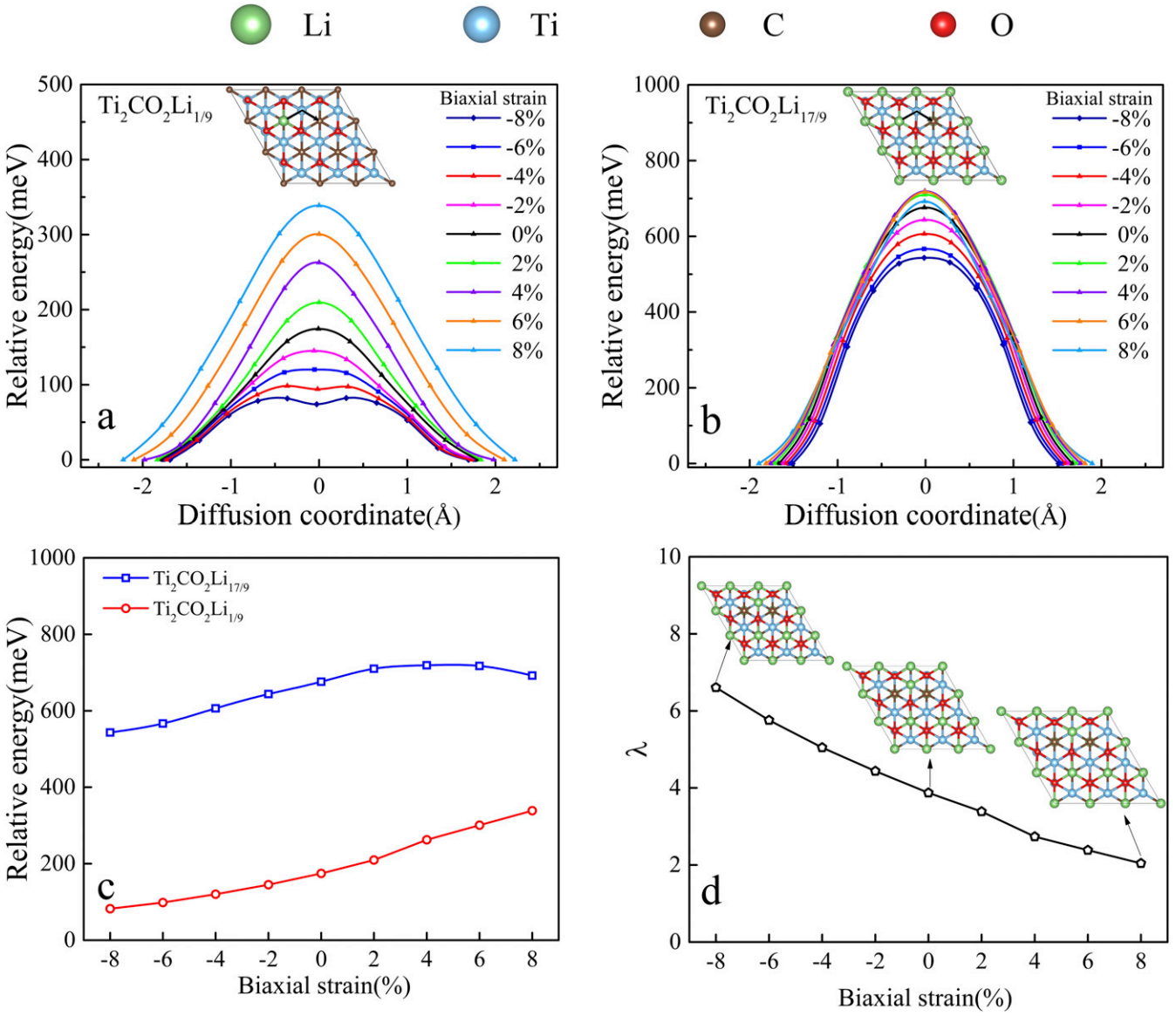

Fig. S12. Potential-energy profiles of Li^+ diffusion on the charged surface of Ti_2CO_2 under biaxial strain with (*A*) low and (*B*) high Li coverage. (*C*) The relationship between barrier and biaxial strain and (*D*) the relationship between λ and biaxial strain.

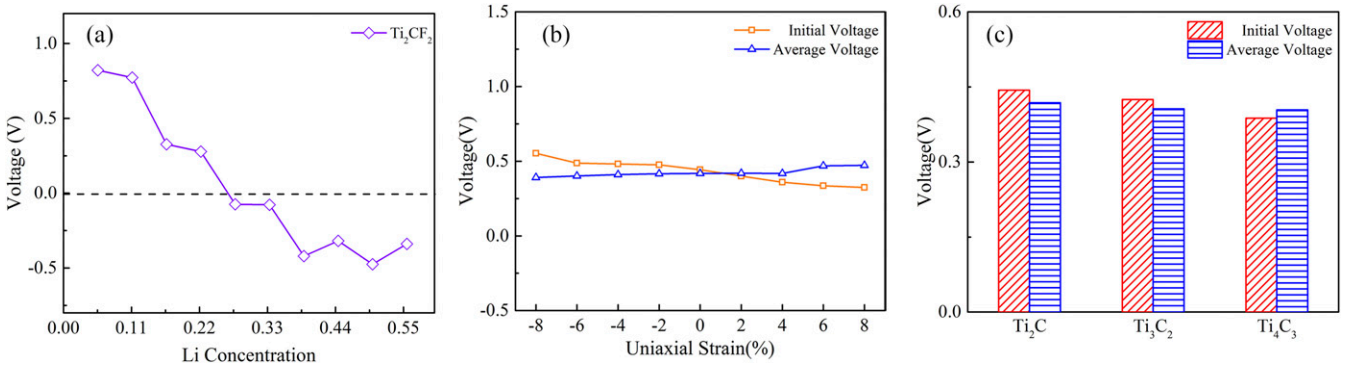

Fig. S13. A voltage profile of (*A*) Ti_2CF_2 along different Li coverages. The initial voltages and the average voltages of (*B*) Ti_2C at the uniaxial strains. (*C*) The initial voltages and the average voltages of Ti_2C, Ti_3C_2, and Ti_4C_3.

Table S1. The energy per primitive cell M_2CT_2 (M = Ti, Zr, T = O, F) of configurations I, II, and III

Configuration	Ti_2CO_2	Ti_2CF_2	Zr_2CO_2	Zr_2CF_2
I	1.74	0.53	1.96	0.34
II	0	0	0	0
III	0.76	0.20	0.87	0.06

The energy of the most stable configuration is set to 0. The energy difference between the most stable configuration and the other configuration is shown.

Table S2. The energy per primitive cell of configurations I, II, and III in Fig. S2

E/eV	Ti_2C	Zr_2C	Hf_2C	Ta_2C	Mo_2C	W_2C	Ti_2CO_2	Ti_2CF_2	Zr_2CO_2	Zr_2CF_2	Ti_3C_2	Ti_4C_3
I	0	0	0	0.39	0.11	0	0	0.03	0	0	0	0
II	0.13	0.14	0.10	0	0	0.08	0.03	0	0.28	0.05	0.05	0.01
III	0.39	0.37	0.44	0.47	0.19	1.57	0.25	0.21	0.34	0.12	0.09	0.06
d_L/Å	4.83	5.34	5.23	4.99	4.69	4.96	6.93	7.10	6.11	7.06	7.27	9.79

The energy of the most stable configuration is set to 0. The energy difference between the most stable configuration and the other configuration is shown. d_L is the layer thickness of the most stable configuration.